Nonlinearity of the cloud response postpones climate penalty of mitigating air pollution in polluted regions

Hailing Jia ⬤ ✉ & Johannes Quaas ⬤

Aerosol–cloud interactions contribute substantially to uncertainties in anthropogenic forcing, in which the sensitivity of cloud droplet number concentration (N_d) to aerosol plays a central role. Here we use satellite observations to show that the aerosol–N_d relation (in log–log space) is not linear as commonly assumed. Instead, the N_d sensitivity decreases at large aerosol concentrations due to the transition from aerosol-limited to updraft-limited regime, making the widely used linear method problematic. A sigmoidal transition is shown to adequately fit the data. When using this revised relationship, the additional warming that arises from air pollution mitigation is delayed by two to three decades in heavily polluted locations, compared to the linear relationship. This cloud-mediated climate penalty will manifest markedly starting around 2025 in China and 2050 in India after applying the strongest air quality policy, underlining the urgency of mitigating greenhouse gas emissions.

Aerosol particles affect Earth's energy balance through exerting effective radiative forcings (ERF_{aer}) via both aerosol–radiation interactions and aerosol–cloud interactions[1]. Specifically, aerosols can alter radiative balance directly by scattering and absorbing sunlight (ERF_{ari}) and also indirectly by acting as cloud condensation nuclei (CCN), in turn modifying cloud properties and precipitation (ERF_{aci};[2–4]). ERF_{aci} has been known as the most uncertain component in anthropogenic forcing, in which the sensitivity of cloud droplet number concentration (N_d) to aerosol plays a fundamental role[5,6].

The latest report by the Intergovernmental Panel on Climate Change provided a best estimate (5 to 95% confidence interval) of the total ERF_{aer} at −1.1 (−1.7 to −0.4) W m^{-2} (ref. [1]). The resulting cooling due to aerosols in turn counteracts about half of the ERF due to CO_2 from 1750 to 2019[7]. To mitigate risks of air pollution, most industrial regions have implemented air quality regulations, for example, emissions reductions in Europe (EU) and North America (NA) since the mid-1980s[8,9] and in China since 2006–2010[10,11]. This could bring additional 'unmasked' warming due to mitigated cooling from aerosols, leading to what has been called a climate 'penalty'[12]. Modelling studies showed that environmental policies induced warming of 0.25 ± 0.12 °C globally from 2015 to 2055[13], 0.35 °C over the eastern

United States from 1980 to 2010[14], 0.45 ± 0.11 °C over EU from 1970 to 2010[15] and 0.12 ± 0.02 °C over East Asia (only attributed to emissions reductions in China) from 2006 to 2017[16]. Interestingly, more recent evidences from multi-satellite observations together with models also show a clear increase in negative ERF_{aer} by 0.1 to 0.3 W m^{-2} from 2001 to 2019, confirming that the climate penalty has now clearly started to happen[17].

To confidently predict the future climate penalty, a better observational constraint on ERF_{aci} is vital because ERF_{aci} contributes most to the uncertainty of ERF_{aer}[18,19]. In this regard, long-term trends in aerosol loading and cloud variables observed by satellites may be particularly helpful. There have been some attempts to link long-term trends in cloud variables with emissions change. Along with the emissions reduction in EU and the United States, N_d declines were observed correspondingly[20–23], while trends in liquid water path and cloud fraction (CF) were not always consistent with emissions change[22,23] due to their large natural variability compared to the variability driven by N_d. Consistent trends in N_d and aerosols were also reported over India (IN)[21,23] and the East China (EC) Sea[22,24,25] but were not evident over China[21,23]. Those findings support theoretical hypotheses[2,3] but only in terms of qualitative consistency in signs across regions[17].

Leipzig Institute for Meteorology, Leipzig University, Leipzig, Germany. ✉e-mail: hailing.jia@uni-leipzig.de

Here our study provides quantitative estimates of the N_d sensitivity from decadal variations via filtering out high-frequency signals. Together with the analyses based on daily variations of aerosol and N_d, this study comes up with a robust depiction of the N_d sensitivity that the aerosol–N_d relation is nonlinear with a saturated N_d under polluted conditions even in log–log scale. This, in turn, suggests that the commonly used ordinary least-squares (OLS) linear fit on ln aerosol–ln N_d (OLS method) might be problematic to accurately predict the N_d change on the basis of aerosol changes. To tackle this, a sigmoidal fit is proposed as a better alternative and then used to describe the past and predict the timing of cloud-mediated climate penalty with future emissions reduction. Furthermore, we show that current climate models have a limited ability to reproduce the past N_d variation, mainly owing to the insufficient representation of the saturation effect. Our findings highlight the importance of improving the estimation of aerosol–cloud interactions from both observational and modelling sides, especially in terms of the nonlinearity of N_d sensitivity.

Observed decadal trends

Unlike qualitatively comparing the consistency between trends in aerosol and cloud variables[17], here we compute the N_d sensitivity from decadal variations in a quantitative sense. To isolate the signal that is solely relevant to decadal emissions change, a de-seasonalization and a locally weighted scatterplot smoothing were used (Methods).

Decadal variations of normalized anthropogenic aerosol emissions, aerosol index (AI) and N_d from 2001 to 2020 over major industrial regions (Supplementary Fig. 1) are shown in Fig. 1. Continuous declines in sulfur (SO_2) emissions are seen with changes, obtained as linear trends, of −5% per year over EU and −9% per year over NA. In contrast, the SO_2 emissions over IN increase throughout the whole period by 4% per year; in EC it has been increasing until around 2008 (11% per year) and decreasing thereafter (−9% per year). Black carbon (BC) and organic carbon (OC) emissions have similar trends as SO_2 but are less pronounced.

Due to the short lifetime of aerosols, the variations of AI—a proxy of fine-mode aerosol concentration—are tightly following the emissions changes (Fig. 1e–l). However, N_d changes are not always consistent with AI, which is mostly aerosol-environment dependent. For relatively clean regions (AI < 0.25), the N_d variations in general well fit aerosol changes; over the rather clean ocean of NAO, a 1:1 N_d-to-AI sensitivity ($S_{AI} = \frac{d \ln N_d}{d \ln AI}$, unitless) is even observed; NA and EUO also have high S_{AI} of 0.49 and 0.57, respectively. An exception is EU, where an increasing AI is seen until 2010, presumably due to the increasing anthropogenic OC emissions (Fig. 1a) and continuous wildfire events[26]. In this case, the AI variation is linked more to increasing non-CCN aerosols (BC and OC) rather than the expected declining CCN (sulfate), hence hampering the S_{AI} estimate. In contrast, for polluted regions, N_d is less responsive to aerosol changes; over IN, a 53% increase in AI from 2001 to 2020 results only in 13% enhancement in N_d. This is particularly severe over EC, where N_d does not change at all with such a strong switch in aerosol trends (135% increase before 2008 and then −95% decline afterwards). Similar behaviours also appear in their adjacent oceans (Fig. 1k–l). The corresponding S_{AI} for those polluted regions are lower than 0.15, much smaller than the lower bound (0.3) given by ref. 6.

In addition to aerosols, clouds also respond to global warming and internal climate variability on interannual and decadal timescales[1], which were reported to largely affect observed trends in CF and liquid water content[27]. To confirm if the N_d changes are solely a manifestation of aerosol impacts so that the decadal variations can be confidently used to calculate S_{AI}, we examine Coupled Model Intercomparison Project Phase 6 (CMIP6) multi-model simulations with external radiative forcing only from greenhouse gases (CMIP6-GHG) and only from natural solar variations and volcanic aerosol (CMIP6-NAT; Supplementary Table 2 includes model information). The negligible

trends (less than 0.05% per year) generated by the two experiments support the idea that aerosol emissions governed N_d changes on a decadal scale.

Implications for N_d sensitivity

It is important to note that S_{AI} is calculated based on decadal variations of regional means, in turn limiting aerosol variability, which ties S_{AI} to a certain aerosol condition. There is a strong negative dependence of S_{AI} on regional mean AI (Fig. 2a). In very polluted regions, which is generally updraft limited, S_{AI} is close to 0, while for relatively clean oceans, which is more likely aerosol limited, it can be almost 1, that is, the maximal value we would expect. This reflects a transition from aerosol-limited to updraft-limited regime with increasing aerosol[28].

However, what we have been doing is to compute the N_d sensitivity as a fixed value with aerosol varying for a specific regime. Here the regimes are mainly used to constrain the co-variability of aerosol type and meteorological background[29]. The problem is, no matter how accurately those regimes can be constrained, as long as S is kept as a constant with the aerosol regime, the aerosol-updraft transition is naturally fixed. But according to the finding here, it is apparently not true. By continuously increasing aerosol, we will eventually go to the updraft-limited regime, for example, the insensitive N_d seen in EC and IN. A reduced S with aerosol increasing or a saturated N_d at high aerosol loading even in log–log scale is thus theoretically expected.

By considering the linear aerosol–N_d relation in logarithmic space, the OLS method can capture the tendency towards saturation as reflected by a power-law relation in regular space, but it is insufficient to capture the absolute saturated N_d under high aerosol loading unless the sensitivity is set to zero. Although this nonlinear ln aerosol–ln N_d relation has been observed in previous studies that used different CCN proxies[30–32], the OLS method was still used to fit the relation. As shown in Fig. 2b (the upper panel), the AI–N_d joint histogram constructed from non-precipitating clouds over global oceans is well characterized by an S shape. Note that the flat N_d under clean conditions is not physically meaningful and instead is caused by the problematic aerosol retrieval[33]. The conventional OLS method is unable to capture the 'shallow' relation on both low and high ends (Fig. 2b). Besides this, the OLS method is sensitive to the probability distribution of aerosol as it puts more weight to commonly occurring aerosol values. This explains why the low sensitivity was often observed over the pristine Southern Ocean[31,34], where a strong N_d response is expected instead.

To overcome the issues raised by the OLS method, we propose using a sigmoidal function to fit the ln AI–ln N_d relation. Here the median N_d in each AI bin is taken as the input of regression, ensuring that the equal weight is put to each AI. It is exciting to see that the sigmoid method perfectly captures the N_d variation. The peak S_{AI} of sigmoid method is 1 at AI = 0.16, which is a demarcation between the aerosol-limited and transition regime, assuming first-order unchanged updraft with aerosol. In the aerosol-limited regime, the reduced S_{AI} was reported as an artefact of the aerosol-retrieval issue[33], thus the plausible value should be 1, given the nature of the aerosol-limited regime[28]. Then, the plausible N_d prediction is inferred accordingly (dotted cyan/grey line in Fig. 2b). This corrected sigmoid curve will be used in the rest of the paper. Surprisingly, in the aerosol-updraft transition regime (AI > 0.16), the S_{AI} from daily variations are overall well consistent with ones derived from decadal trends—decreasing sensitivity as aerosol increases, except for EU, where the AI variation cannot reflect the CCN decadal trend. The two lines of evidence confirm the nonlinearity of ln AI–ln N_d relation.

Capturing this nonlinearity is crucially important when predicting N_d evolution and/or estimating radiative forcing due to aerosol–cloud interactions (RF$_{aci}$). According to the observations, N_d starts to be largely saturated around AI = 0.35, but the OLS method gives a continuously increasing N_d (Fig. 2c). This means that the OLS method tends to overestimate N_d change from pre-industrial (PI) to present day (PD)

Fig. 1 | Decadal variations of emissions, aerosol index and cloud droplet number concentration during 2001–2020 over major industrial regions and their adjacent oceans. a–d, Anthropogenic SO_2, BC and OC emissions from the Community Emissions Data System (CEDSv_2021_04_21;[44]) over EU (**a**), NA (**b**), IN (**c**) and EC (**d**). e–h, AI and N_d from MODIS, N_d from CMIP6 hist/ssp245-GHG and hist/ssp245-NAT experiments over EU (**e**), NA (**f**), IN (**g**) and EC (**h**). i–l, Same as **e**–**h** but for adjacent oceans: EUO (**i**), NAO (**j**), INO (**k**) and ECO (**l**). Here the variables are normalized against the 20-year mean value in each region, meaning the percent deviation from the mean value (in units of %). The time series are smoothed using robust locally weighted regression algorithm (LOWESS) with a seven-year time window. The numbers in the top right corner of each plot show relative trends (% per year). The corresponding multi-year means and absolute linear trends are displayed in Supplementary Table 1. Also shown is the N_d sensitivity (S_{AI}) calculated from decadal variations of AI and N_d excluding any high-frequency noises.

over very polluted regions, while underestimating it over moderately polluted regions, which would bias the spatial patterns of N_d change[30] and hence RF_{aci}[34–36].

Past and future trends in N_d and RF_{aci}

The OLS method has been often employed to estimate the PD–PI N_d change (ΔN_d) and RF_{aci}, however, it is difficult to evaluate its accuracy due to the impossibility of observing the PI N_d. In this regard, satellite-observed N_d trends over past decades provide a great opportunity to evaluate the predictability of OLS and sigmoid methods. Moreover, the future trends are also of particular interest. As recently documented by ref. 17, on a global scale, the reduction in aerosol emissions since 2000 brought additional warming radiative effects through both direct and indirect effects. Nevertheless, at a regional scale over China, we do not actually see the climate penalty mediated by the indirect effects, as N_d nearly did not change because of the saturation effect at high aerosol. It is expected that with the future emissions reduction,

the climate penalty will eventually manifest at increasing rates. Thus, what is interesting now is when this will happen.

The agreement between the AI predicted by the historical SO_2 emissions and observed by MODerate Resolution Imaging Spectroradiometer (MODIS) lends credibility to future AI predictions (Fig. 3). From these, in turn, the transient changes in N_d can be inferred. The OLS-diagnosed N_d strongly scales with aerosol changes (Fig. 3b,e) and thereby is unable to reproduce the saturated (slightly increasing) N_d over EC (IN) in the past. Also, for the SSP2–4.5 and SSP3–7.0 pathways in IN, where the AI remains higher than the critical AI (Fig. 3d and Extended Data Fig. 1), the updraft-limited behaviours are expected, however, the OLS-diagnosed N_d is still highly sensitive to aerosol.

It is interesting to see that the sigmoid method performs very well in reproducing the past trends over each region—not only the saturated N_d in EC and IN (Fig. 3b,e) but also strong declines in NA and EU (Extended Data Fig. 2). Looking at the near-term future, the sigmoid-diagnosed N_d stay almost unchanged under the scenarios
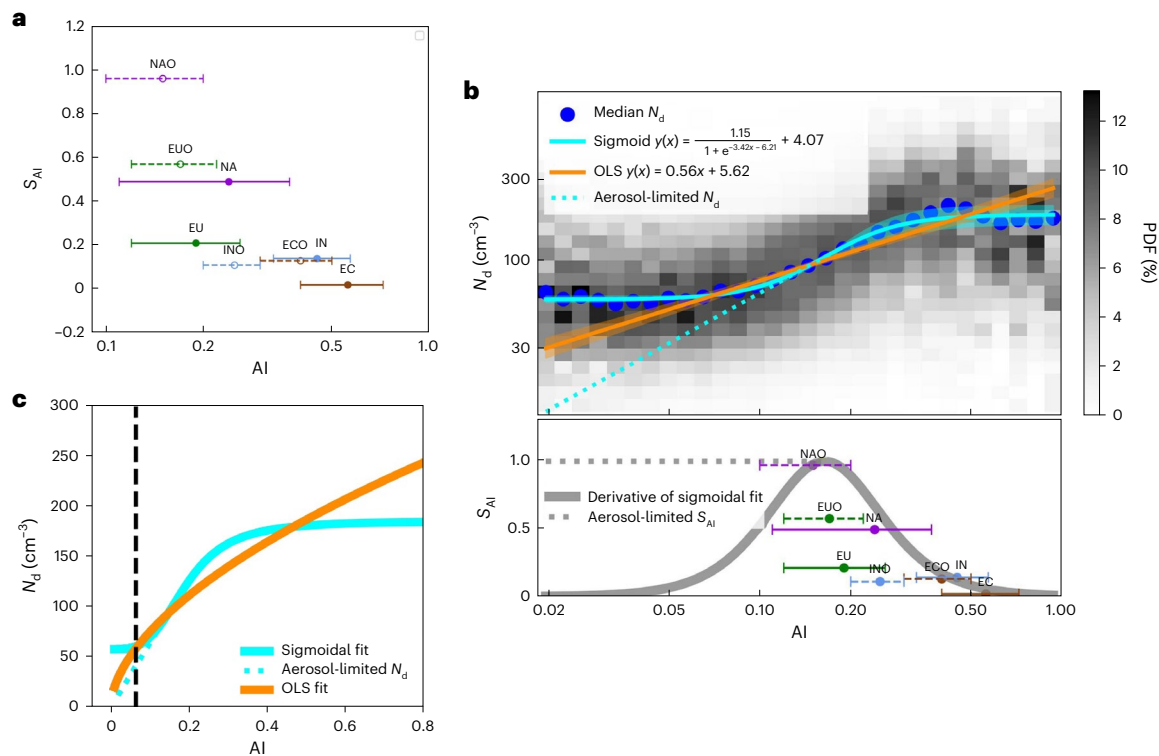
Fig. 2 | Observed relationships between aerosol index and cloud droplet number concentration and implied N_d sensitivity. a, Dependence of S_{AI} on AI, where S_{AI} is inferred from decadal variations and the mean ± standard deviation (error bar) of AI is calculated based on 20-year annual means (sample sizes $n = 20$) for each region. **b**, The upper panel depicts the joint AI–N_d histogram constructed from 5 km × 5 km daily observations of non-precipitating liquid clouds over global oceans, where each column is normalized so that it sums to 1. The blue dot indicates the median N_d in each AI bin. Also shown are OLS linear and sigmoidal fits on blue dots ($n = 30$), with the shaded area representing the 95% credible interval (according to a Student's t test) that represents the fitting uncertainty. Corresponding fitting functions are displayed as well where $x = \ln$ AI and $y = \ln N_d$. The lower panel in **b** shows the derivative of the sigmoidal fit

function that is equivalent to S_{AI}, along with the dependence of S_{AI} on AI shown in **a**. **c**, Schematic explaining the advantage of sigmoid method over OLS method in capturing N_d change with AI. The vertical black dashed line is at an AI of 0.05, with unreliable aerosol retrievals lying to the left of the line[31]. The dotted cyan and grey curves in **b** and **c** indicate the plausible predictions considering the issue of large retrieval error under clean conditions. Data used to generate **a** are 20-year observations (2001–2020) of AI and N_d from MODIS Level 3 1° × 1° products. Data used to construct **b** and **c** are one-year (2008) MODIS 5 × 5 km² daily N_d and AI (interpolated from 1° × 1°) observations over global oceans between 60° S and 60° N, in which the 2B-CLDCLASS product[45] from CloudSat radar is utilized to exclude precipitation pixels to reduce uncertainty.

SSP3–7.0 for EC and the SSP2–4.5 and SSP3–7.0 for IN. When going to the cleanest scenarios (SSP1–2.6), the decline in N_d would occur around 2025 in EC and 2050 in IN. The regression uncertainty can alter the predicted year by ten years for EC (2020–2030) and seven years for IN (2045–2052) (Fig. 3a,d).

The N_d changes are consequently reflected in RF$_{aci}$ evolutions. The strong changes in aerosol emissions in EC over the past two decades did not exert any appreciable RF$_{aci}$ (Fig. 3c). Similarly in IN, the strong sulfur emissions resulted in a regional mean RF$_{aci}$ of merely –0.45 W m^{-2} by 2020 relative to 2001 (Fig. 3f). However, for the regions that already transited out of the updraft-limited regime due to air quality policy implementations (including NA and EU in Extended Data Fig. 2), aerosol reductions efficiently led to stronger warming with RF$_{aci}$ of 1.37 W m^{-2} and 0.91 W m^{-2} by 2020, respectively.

According to the sigmoid-based predictions, if the strongest air quality policy (SSP1–2.6) will be applied, the rapid warming via RF$_{aci}$ are estimated to occur around 2025 in EC and 2050 in IN (the same time as N_d falling), with ~17 and ~30 years delayed compared to the conventional OLS predictions. Note that we considered aerosol-limited $S_{AI} = 1$ in the sigmoidal prediction. Sensitivity experiments further show that the diverse treatments of aerosol-limited S_{AI} lead to spreads in the RF$_{aci}$ of ~1–2 W m^{-2} at 2100 (Supplementary Fig. 2), but this does not affect the prediction of timing when the climate penalty will occur. Similarly, the warming in EC will be postponed by ~22 years under SSP2–4.5; but under

SSP3–7.0, no additional forcing will be imposed to EC and IN owing to the saturated N_d. Beyond this delayed warming in polluted regions, the sigmoidal predictions reveal an accelerated warming in clean regions (NA and EU), with nearly double increase rates in RF$_{aci}$ relative to the OLS results (Extended Data Fig. 2). As cloud adjustments approximately scale with RF$_{aci}$[6,37], the predicted evolutions are relevant for ERF$_{aci}$, too.

Performance of CMIP6 models in reproducing N_d trends

Modelling studies demonstrated enhanced future warming and precipitation from aerosol reductions[14,16]. However, the lack of a proper representation of the observed nonlinearity of the N_d response to aerosols (in log–log space) in climate models may imply they overestimate the warming from aerosol reductions in polluted regions that are still in the updraft-limited regime. For example, the climate models suggested a regional ERF$_{aer}$ of ~3 W m^{-2} induced by emissions reductions during 2006–2017 over EC, along with strong enhancements of surface air temperature (~0.3 °C) and precipitation (~70 mm per year) (ref. 16). Such strong climate effects are unlikely to occur in the absence of aerosol indirect forcing, as it contributes the largest part of ERF$_{aer}$[1,6].

Therefore, it is essential to evaluate the performance of current climate models in reproducing observed N_d trends. We see that none of the CMIP6 models can reproduce the observed unchanged N_d trends in EC (Fig. 4). Though some models perform better for the regions
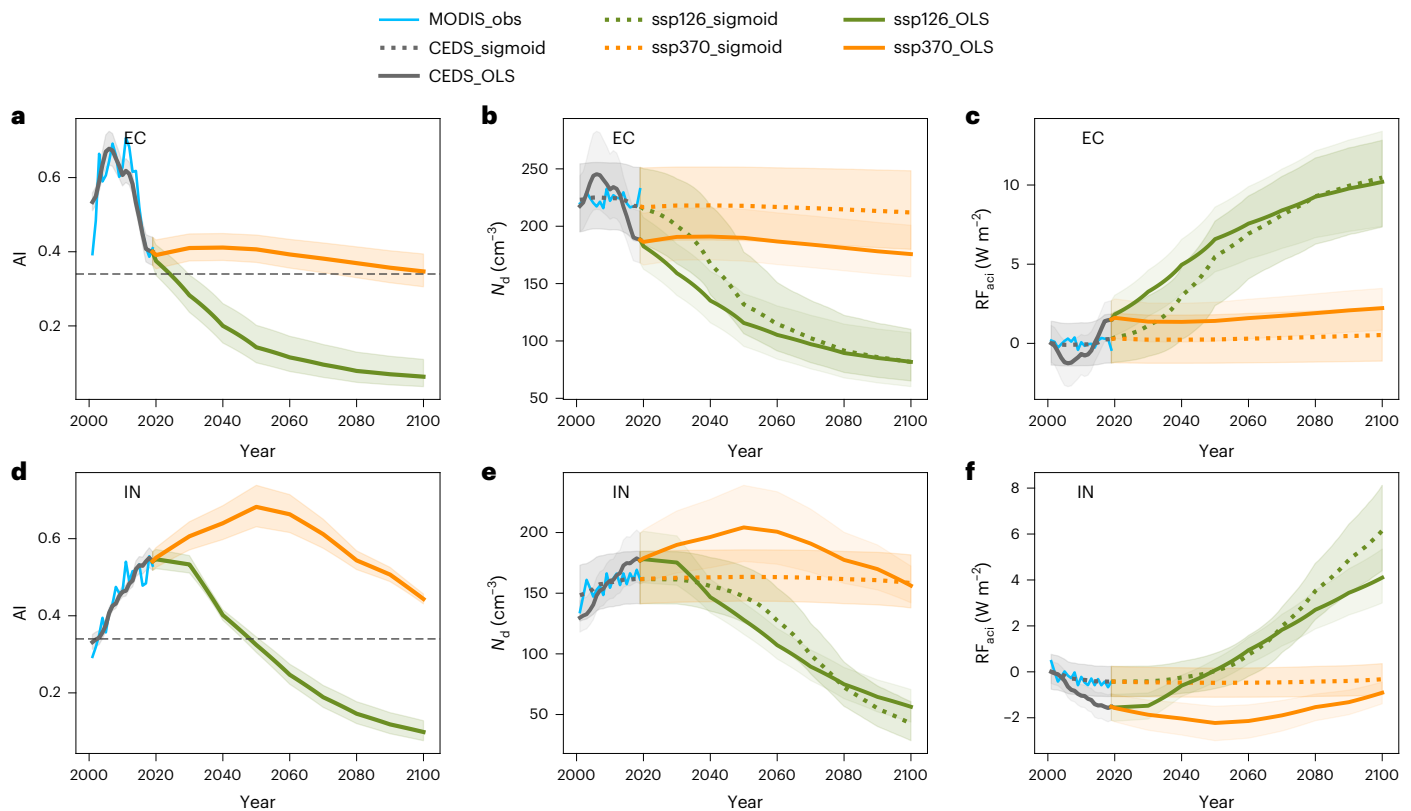
Fig. 3 | Observed and predicted aerosol index, cloud droplet number concentration and radiative forcing during 2000–2100. a–f, Past and future mean regional changes in AI (**a**,**d**), N_d (**b**,**e**) and RF_{aci} (**c**,**f**) over EC (top) and IN (bottom) diagnosed from past (grey) and future aerosol emissions under strong-mitigation (SSP1–2.6; green) and high-emissions (SSP3–7.0; orange) scenarios. To enhance the conciseness and readability, the results for mid-emissions (SSP2–4.5) are not displayed here and instead are shown in Extended Data Fig. 1. Historical observations of AI and N_d from MODIS Level 3 1° × 1° products (2001–2020) are shown in cyan. Solid and dashed lines indicate the predictions using OLS and sigmoid methods, respectively, for N_d and RF_{aci}, with the shaded areas representing the 95% confidence interval (according to a Student's *t* test) that represents the regression uncertainty. The horizontal dashed lines in **a** and **d** denote the critical AI (0.35) from the sigmoidal fit in Fig. 2b, below which the updraft-limited regime is transiting towards the aerosol-limited regime, that is, the aerosol effect starts to appear. Here the critical AI is defined as the AI value when S_{AI} equals to 0.2, in which case the aerosol effect on N_d is assumed to be negligible.

where N_d is not completely saturated (IN, NA and EU), the majority of models still tend to systematically overestimate the relative changes compared to observations and sigmoid-based predictions. Under the future polluted scenario (SSP3–7.0), the saturated N_d is expected over EC and IN (Supplementary Fig. 3), according to our analysis, but the CMIP6 models instead show fairly strong N_d changes.

When focusing on models that have the same dynamical core, turbulent diffusion and cloud microphysics but only differ in activation treatments (green shaded areas), it is clear that the detailed activation scheme consistently performs better than the OLS empirical parameterization. The detailed activation scheme accounts for the depletion of the maximum supersaturation under high aerosol loading[38], thus allowing the simulation of the reduced N_d sensitivity with more aerosol abundance[39,40] to some extent. This, however, is still insufficient to fully capture the nonlinearity as observed by satellites.

Discussion

Our results based on both decadal and daily variations demonstrate that the aerosol–N_d relation even in log–log space is not linear as commonly assumed. Specifically, the N_d sensitivity is shown to be negatively correlated with aerosol loading in a region, indicating a transition from aerosol-limited to updraft-limited regime with aerosol increasing. This finding suggests that the widely used OLS method and corresponding RF_{aci} estimate[30,34–36] are problematic because they assume a constant N_d sensitivity despite the mean aerosol varying.

As a step forward, a sigmoidal function is proposed and shown to fit the S-shaped ln AI–ln N_d relation seen by satellite statistics. The optimized sigmoid method overcomes two major issues: (1) the non-linearity of the ln aerosol–ln N_d relation and (2) the poor retrieval capability under clean conditions, which drives part of the uncertainty in aerosol–cloud radiative forcing[39,41]. As a result, the sigmoid method performs very well in reproducing the past N_d trends—not only the saturated N_d in EC and IN but also strong declines in NA and EU, lending credibility to the near-term N_d and RF_{aci} predictions.

Although the cloud-mediated climate penalty of air quality improvements was not observed in EC over past decades because of the saturation effect, it is expected to manifest eventually with future mitigation of air pollution (scenario SSP1–2.6). According to the sigmoid-based predictions, the rapid warming via RF_{aci} is estimated to start occurring from around 2025 in EC and from 2050 in IN. In relatively clean regions (NA and EU), the sigmoid-based predictions show much larger increasing rates in RF_{aci} compared to the conventional OLS method. This highlights the urgency of mitigating greenhouse gas emissions to avoid strong temperature increase rates.

ERF_{aci} can be faithfully projected only if the historical N_d evolution is faithfully simulated. However, we show that none of the CMIP6 models can reproduce the saturated N_d over EC satisfactorily. Generally, the majority of models tend to overestimate the relative changes of N_d. Although the detailed activation scheme is better than the OLS empirical parameterization, it is still insufficient. Failure to simulate the
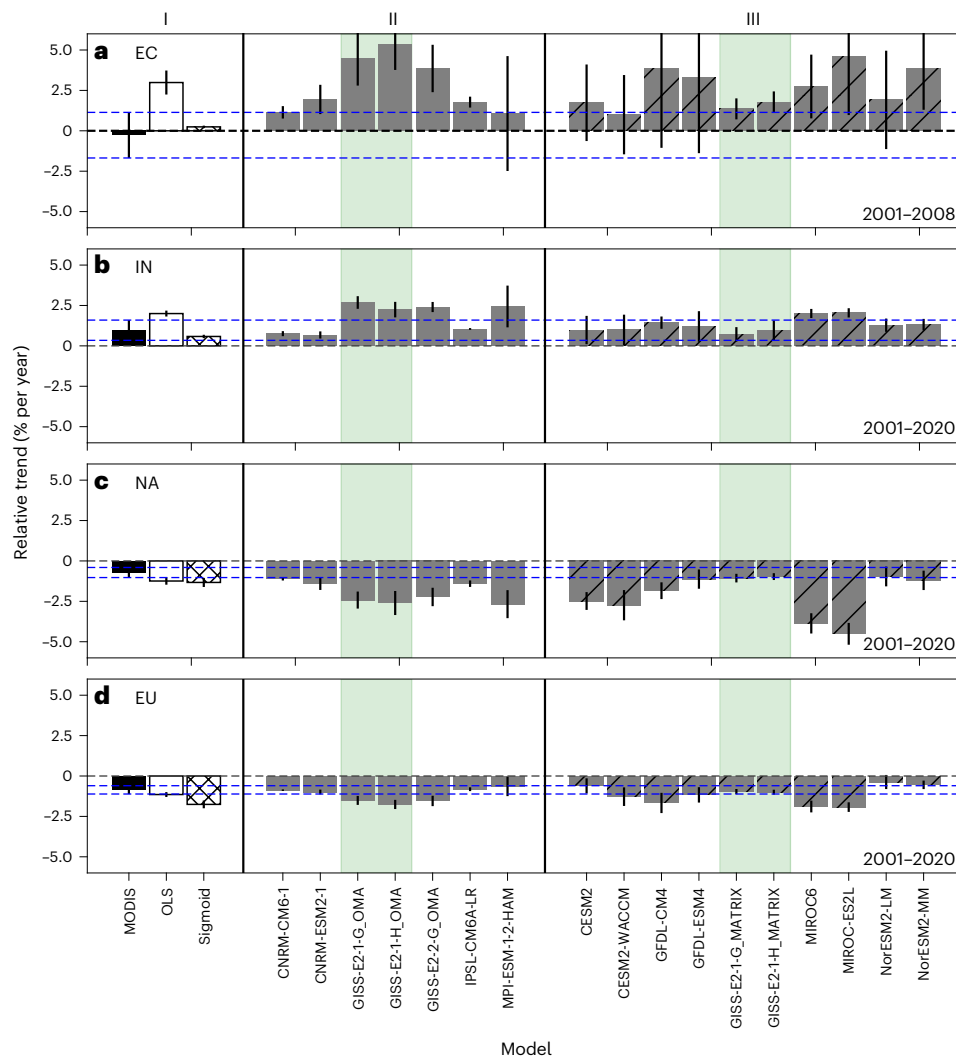
Fig. 4 | Linear trends in cloud droplet number concentrations from MODIS, observation-based predictions and CMIP6 models. Trends in N_d retrieved from MODIS Level 3 1° × 1° products and predicted by OLS and sigmoid regression methods (group I) and simulated by 17 CMIP6 models with empirical parameterizations (group II) and detailed activation schemes (group III), along with 95% confidence intervals (according to a Student's t test) depicted as error bars. **a**–**d**, The whole period of 2001–2020 ($n = 20$) is chosen for calculating the trends in IN (**b**), NA (**c**) and EU (**d**), but 2001–2008 ($n = 8$) for EC (**a**), because from 2008 onwards, there was a trend reversal and also the SO_2 emissions used in CMIP6 models were incorrect[46]. Blue dashed lines highlight the 95% confidence intervals of trends from MODIS. Green shaded areas mark GISS-E2-1-G/H models that have both the empirical parameterization (OMA) and the advanced activation scheme (MATRIX).

saturation effect might explain why climate models suggest stronger cooling from aerosols in the 1970s[42]. The findings here emphasize that further improvements to the current activation scheme are needed to achieve better ERF_aci projections.

A few potential caveats to the sigmoid predictions should be noted. Considering the large uncertainties in retrievals over land, the sigmoidal curve was inferred from well-filtered single-layer liquid clouds over the global ocean. The cost of retrieval quality is to discard a portion of clouds, which is acceptable compared to the large confounding effects caused by retrieval errors[32,43]. Additionally, the differing backgrounds of meteorological conditions and aerosol types among regions might lead to a difference in the threshold of AI for the updraft-limited regime that cannot be reflected in the current sigmoidal fit. However, this effect appears small (Supplementary Fig. 4). The reproduction of historical N_d trends over land largely supports the utility of this sigmoidal relationship over land. However, to thoroughly fix the above issues, using improved CCN and cloud retrievals over land[31] and constraining updraft regimes[32] would be useful ways forward. Additionally, to eliminate the confounding effect of precipitation on

the aerosol–N_d relation, only non-precipitating clouds were analysed, so the sigmoid-based N_d and RF_aci projections did not account for the impact of changing precipitation under global warming. Although those caveats might add uncertainties or alter the predicted year when the climate penalty will occur, it does not hamper the robustness of the optimized sigmoidal fit as a promising alternative for the conventional OLS method that has been shown to be problematic.

Online content

Any methods, additional references, Nature Portfolio reporting summaries, source data, extended data, supplementary information, acknowledgements, peer review information; details of author contributions and competing interests; and statements of data and code availability are available at https://doi.org/10.1038/s41558-023-01775-5.

References

1. Forster, P. et al. in *Climate Change 2021: The Physical Science Basis* (eds Masson-Delmotte, V. et al.) 923–1054 (Cambridge Univ. Press, 2021).

2. Twomey, S. Pollution and the planetary albedo. *Atmos. Environ.* **8**, 1251–1256 (1974).

3. Albrecht, B. A. Aerosols, cloud microphysics, and fractional cloudiness. *Science.* **245**, 1227–1230 (1989).

4. Ackerman, A. S., Kirkpatrick, M. P., Stevens, D. E. & Toon, O. B. The impact of humidity above stratiform clouds on indirect aerosol climate forcing. *Nature.* **432**, 1014–1017 (2004).

5. Boucher, O. et al. in *Climate Change 2013: The Physical Science Basis* (eds Stocker, T. et al.) 571–658 (Cambridge Univ. Press, 2013).

6. Bellouin, N. et al. Bounding global aerosol radiative forcing of climate change. *Rev. Geophys.* **58**, e2019RG000660 (2020).

7. Szopa, S. et al. in *Climate Change 2021: The Physical Science Basis* (eds Masson-Delmotte, V. et al.) 817–922 (Cambridge Univ. Press, 2021).

8. Vestreng, V., Myhre, G., Fagerli, H., Reis, S. & Tarrasón, L. Twenty-five years of continuous sulphur dioxide emission reduction in Europe. *Atmos. Chem. Phys.* **7**, 3663–3681 (2007).

9. Aas, W. et al. Global and regional trends of atmospheric sulfur. *Sci. Rep.* **9**, 953 (2019).

10. Lu, Z., Zhang, Q. & Streets, D. G. Sulfur dioxide and primary carbonaceous aerosol emissions in China and India, 1996–2010. *Atmos. Chem. Phys.* **11**, 9839–9864 (2011).

11. Zheng, B. et al. Trends in China's anthropogenic emissions since 2010 as the consequence of clean air actions. *Atmos. Chem. Phys.* **18**, 14095–14111 (2018).

12. Ekman, A. et al. *Is There a Conflict Between the Clean Air Goals of the European Green Deal and Climate Neutrality?* (Forces, 2020); https://forces-project.eu/publications/policy-brief

13. Allen, R. J. et al. Climate and air quality impacts due to mitigation of non-methane near-term climate forcers. *Atmos. Chem. Phys.* **20**, 9641–9663 (2020).

14. Leibensperger, E. M. et al. Climatic effects of 1950–2050 changes in US anthropogenic aerosols–part 2: climate response. *Atmos. Chem. Phys.* **12**, 3349–3362 (2012).

15. Turnock, S. T. et al. The impact of European legislative and technology measures to reduce air pollutants on air quality, human health and climate. *Environ. Res. Lett.* **11**, 024010 (2016).

16. Zheng, Y., Zhang, Q., Tong, D., Davis, S. J. & Caldeira, K. Climate effects of China's efforts to improve its air quality. *Environ. Res. Lett.* **15**, 104052 (2020).

17. Quaas, J. et al. Robust evidence for reversal of the trend in aerosol effective climate forcing. *Atmos. Chem. Phys.* **22**, 12221–12239 (2022).

18. Smith, C. J. et al. Effective radiative forcing and adjustments in CMIP6 models. *Atmos. Chem. Phys.* **20**, 9591–9618 (2020).

19. Thornhill, G. D. et al. Effective radiative forcing from emissions of reactive gases and aerosols–a multi-model comparison. *Atmos. Chem. Phys.* **21**, 853–874 (2021).

20. Krüger, O. & Graßl, H. The indirect aerosol effect over Europe. *Geophys. Res. Lett.* **29**, 31-1–31-4 (2002).

21. Li, J. et al. Long-term variation of cloud droplet number concentrations from space-based lidar. *Remote Sens. Environ.* **213**, 144–161 (2018).

22. Bai, H., Wang, M., Zhang, Z. & Liu, Y. Synergetic satellite trend analysis of aerosol and warm cloud properties ver ocean and its implication for aerosol-cloud interactions. *J. Geophys. Res. Atmos.* **125**, e2019JD031598 (2020).

23. Cherian, R. & Quaas, J. Trends in AOD, clouds and cloud radiative effects in satellite data and CMIP5 and CMIP6 model simulations over aerosol source regions. *Geophys. Res. Lett.* **47**, e2020GL087132 (2020).

24. Bennartz, R., Fan, J., Rausch, J., Leung, L. R. & Heidinger, A. K. Pollution from China increases cloud droplet number, suppresses rain over the East China Sea. *Geophys. Res. Lett.* **38**, 9704 (2011).

25. McCoy, D. T. et al. Predicting decadal trends in cloud droplet number concentration using reanalysis and satellite data. *Atmos. Chem. Phys.* **18**, 2035–2047 (2018).

26. Filonchyk, M., Hurynovich, V. & Yan, H. Trends in aerosol optical properties over Eastern Europe based on MODIS-Aqua. *Geosci. Front.* **11**, 2169–2181 (2020).

27. Norris, J. R. et al. Evidence for climate change in the satellite cloud record. *Nature* **536**, 72–75 (2016).

28. Reutter, P. et al. Aerosol- and updraft-limited regimes of cloud droplet formation: influence of particle number, size and hygroscopicity on the activation of cloud condensation nuclei (CCN). *Atmos. Chem. Phys.* **9**, 7067–7080 (2009).

29. Stevens, B. & Feingold, G. Untangling aerosol effects on clouds and precipitation in a buffered system. *Nature* **461**, 607 (2009).

30. McCoy, D. T. et al. The global aerosol-cloud first indirect effect estimated using MODIS, MERRA, and AeroCom. *J. Geophys. Res. Atmos.* **122**, 1779–1796 (2017).

31. Hasekamp, O. P., Gryspeerdt, E. & Quaas, J. Analysis of polarimetric satellite measurements suggests stronger cooling due to aerosol-cloud interactions. *Nat. Commun.* **10**, 5405 (2019).

32. Jia, H., Quaas, J., Gryspeerdt, E., Böhm, C. & Sourdeval, O. Addressing the difficulties in quantifying droplet number response to aerosol from satellite observations. *Atmos. Chem. Phys.* **22**, 7353–7372 (2022).

33. Ma, P.-L., Rasch, P. J., Chepfer, H., Winker, D. M. & Ghan, S. J. Observational constraint on cloud susceptibility weakened by aerosol retrieval limitations. *Nat. Commun.* **9**, 2640 (2018).

34. Jia, H., Ma, X., Yu, F. & Quaas, J. Significant underestimation of radiative forcing by aerosol-cloud interactions derived from satellite-based methods. *Nat. Commun.* **12**, 3649 (2021).

35. Kinne, S. Aerosol radiative effects with MACv2. *Atmos. Chem. Phys.* **19**, 10919–10959 (2019).

36. Diamond, M. S., Director, H. M., Eastman, R., Possner, A. & Wood, R. Substantial cloud brightening from shipping in subtropical low clouds. *AGU Adv.* **1**, e2019AV000111 (2020).

37. Gryspeerdt, E. et al. Surprising similarities in model and observational aerosol radiative forcing estimates. *Atmos. Chem. Phys.* **20**, 613–623 (2020).

38. Abdul-Razzak, H. & Ghan, S. J. A parameterization of aerosol activation: 2. multiple aerosol types. *J. Geophys. Res. Atmos.* **105**, 6837–6844 (2000).

39. Gryspeerdt, E. et al. Constraining the instantaneous aerosol influence on cloud albedo. *Proc. Natl Acad. Sci. USA* **114**, 4899–4904 (2017).

40. Zhang, K. et al. Effective radiative forcing of anthropogenic aerosols in E3SM version 1: historical changes, causality, decomposition, and parameterization sensitivities. *Atmos. Chem. Phys.* **22**, 9129–9160 (2022).

41. Gryspeerdt, E. et al. Uncertainty in aerosol–cloud radiative forcing is driven by clean conditions. *Atmos. Chem. Phys.* **23**, 4115–4122 (2023).

42. Golaz, J.-C. et al. The DOE E3SM model version 2: Overview of the physical model and initial model evaluation. *J. Adv. Model. Earth Syst.* **14**, e2022MS003156 (2022).

43. Jia, H., Ma, X., Quaas, J., Yin, Y. & Qiu, T. Is positive correlation between cloud droplet effective radius and aerosol optical depth over land due to retrieval artifacts or real physical processes? *Atmos. Chem. Phys.* **19**, 8879–8896 (2019).

44. O'Rourke, P. et al. CEDS v_2021_04_21 gridded emissions data. United States. Datahub https://doi.org/10.25584/PNNLDataHub/1779095 (2021).

45. Sassen, K. & Wang, Z. Classifying clouds around the globe with the CloudSat radar: 1-year of results. *Geophys. Res. Lett.* **35**, L04805 (2008).

46. Wang, Z. et al. Incorrect Asian aerosols affecting the attribution and projection of regional climate change in CMIP6 models. *npj Clim. Atmos. Sci.* **4**, 2 (2021).

Methods

Aerosol and N_d observations

Level 3 1° × 1° products of the MODIS Collection 6.1 (MOD08 and MYD08) provide aerosol optical depth (AOD) and Ångström exponent (AE) retrieved at several wavelengths globally[47,48]. In this study, the AOD is from Dark Target and Deep Blue combined product. Compared to AOD, the AI is considered a better proxy for CCN because it is more weighted towards smaller particles[49,50]. The AI is derived from AOD and Ångström exponent (AI = AOD × AE), in which AE is calculated from AOD at wavelengths of 460 and 660 nm. To minimize the influence of heterogeneous aerosol distribution, we discarded aerosol retrievals where the relative standard deviation is larger than unity[51].

Cloud droplet effective radius (CER) and cloud optical depth from the MODIS Level 2 products (MOD06 and MYD06;[52]) are used to calculate N_d based on the adiabatic approximation[53]. The retrievals at 3.7 μm are used as expected to produce more accurate CER retrievals in inhomogeneous conditions[54]. The following sampling strategy is applied to obtain confident retrievals, that is, only including single-layer liquid clouds with (1) cloud-top temperature higher than 268 K, (2) CER > 4 μm and cloud optical depth > 4 to reduce the uncertainty in weak optical signal conditions[53], (3) CF at 5 km resolution > 0.9 and sub-pixel inhomogeneity index (cloud_mask_SPI) < 30 to reduce the retrieval errors in broken cloud inhomogeneous conditions[54] and (4) solar zenith angle < 65° and sensor zenith angle < 41.4° to minimize the uncertainties raised by cloud 3D effects and multiple scattering[55].

The 2B-CLDCLASS product[45] from CloudSat radar for the year 2008 is employed to identify precipitation. The precipitation data at a 1.4 × 2.5 km² resolution are matched to the nearest MYD06 5 × 5 km² pixels to obtain co-located precipitation flag and N_d. To exclude the possible confounding effect of aerosol–precipitation interactions on N_d sensitivity estimate[32], only non-precipitating clouds (with the flag of 'no precipitation') are analysed to generate the AI–N_d joint histogram, which is then used for linear and sigmoidal fits between AI and N_d.

For the analysis on long-term trends, aerosol and cloud observations in the morning (MOD08 and MOD06 from Terra for 2001–2020) and afternoon (MYD08 and MYD06 from Aqua for 2002–2020) are averaged to represent daily-mean conditions. However, for the AI–N_d joint histogram (Fig. 2b) that is used for the predictions, the simultaneous precipitation observation from CloudSat is necessary for excluding precipitating clouds, thus only observations from the A-Train constellation of satellites in the afternoon (2B-CLDCLASS, MYD08 and MYD06 from CloudSat and Aqua for 2008) are used. We show that one-year data are sufficient to capture the sigmoidal relationship with only a slight change in the statistics compared to the analysis on a longer period (Supplementary Fig. 5).

Emissions data

For the historical period (2001–2019), anthropogenic emissions of sulfur dioxide (SO_2), OC and BC are obtained from the newest version of the Community Emissions Data System (CEDSv_2021_04_21;[44]). An important update compared to the old version of CEDS used in CMIP6[56] is a correction on aerosol emissions trends in China. Comparing to somewhat unchanged SO_2 in the old CEDS from 2006 onwards, the newest version is able to capture strong declines in reality[44].

For the future period (2020–2100), anthropogenic aerosol emissions from different shared socio-economic pathway (SSP) scenarios are used[57], including the low-emission SSP1–2.6 ('sustainability'), intermediate SSP2–4.5 ('middle of the road') and high-emissions SSP3–7.0 ('regional rivalry') scenarios. Notably, the officially released SSP emissions are harmonized to old CEDS emissions (CEDS-v2017-05-18) in the year 2015[58], which causes a discontinuity in the emissions between the newest CEDS data and the future scenarios. To perform a consistent analysis, we thus utilize the software Aneris[59] to harmonize regional-integrated SSP emissions trajectories to the newest CEDS; the methodology of Aneris are described by ref. 60.

Climate model data

The N_d simulated by climate models are taken from CMIP6 'historical', 'hist-GHG' and 'hist-NAT' experiments for the period 2001–2014[61,62] and then extended by the Scenario Model Intercomparison Project (ScenarioMIP) 'sspxxx', 'ssp245-GHG' and 'ssp245-NAT' experiments until 2100[63]. Here 'sspxxx' means different SSP scenarios (SSP1–2.6, SSP2–4.5 and SSP3–7.0). The 'historical' and 'sspxxx' experiments are driven by all forcings, whereas 'hist-GHG' and 'ssp245-GHG' experiments only by greenhouse gas forcing and 'hist-NAT' and 'ssp245-NAT' experiments only by natural forcing. Due to the difficulty in determining the top height of liquid clouds from CMIP6 outputs, alternatively, we make use of the maximal N_d in a vertical atmospheric column to compare with the cloud-top N_d from satellite[64]. To investigate the impact of aerosol activation treatments on the simulated trend in N_d, the models are further divided into two subsets that using: (1) empirical approach that directly links N_d to aerosol concentration and (2) detailed activation schemes, respectively. The details of CMIP6 models analysed in this study are given in Supplementary Table 2.

Isolating decadal signal from high-frequency noise

The systematic change in anthropogenic aerosol emissions occurred over a quasi-decadal timescale. To identify the aerosol–cloud signals solely related to the decadal emissions change, possible noises (that is, high-frequency variability) need to be excluded, specifically (1) the seasonality caused by co-varied meteorological fields and emissions and (2) the occasional fluctuation due to natural emissions, for example, volcano eruptions, wild fires and dust storms. To eliminate (1), we first aggregate the filtered daily AI and N_d into monthly means at each grid point and then remove the monthly cycle from the monthly series by subtracting the difference value between monthly climatology and full-period mean. After regional averaging, we obtain a de-seasonalized monthly series with sample size of 240 (12 months × 20 years) for each grid point. Furthermore, the locally weighted scatterplot smoothing (LOWESS) method is applied to the de-seasonalized series to exclude (2). At each data point, LOWESS conducts a weighted regression within a prescribed span width that determines the number of nearby data used in each local fit[65]. The choice of span width depends on the timescales of interest; here a seven-year time window is chosen to smooth out high-frequency noise. It is illustrated in Supplementary Fig. 6 that the derived N_d sensitivities only change slightly if a different time window is chosen (for example, 4 and 14 years).

Regression models for capturing aerosol–N_d relation

Two regression models are employed to fit aerosol–N_d relations in this study. The first model is the widely used OLS linear regression

$$\ln N_d = \beta \ln \alpha + c \tag{1}$$

where β is the sensitivity of N_d to CCN proxy, α. The OLS method describes a power-law relationship between aerosol and N_d, which has been broadly observed by in situ aircraft measurements, ground- and satellite-based remote sensing, however, mostly over clean to moderately polluted regions[66]. The second model is a sigmoidal regression

$$\ln N_d = \frac{a_1}{1 + e^{a_2 \ln \alpha + a_3}} + a_4 \tag{2}$$

which has a characteristic S-shaped curve, thereby is able to capture the markedly saturated N_d at high aerosol as seen in satellite observations[30–32,41].

N_d prediction

The key idea of predicting N_d from an observational perspective is to bridge two connections: (1) anthropogenic aerosol emissions to aerosol

and (2) aerosol to N_d, by which future aerosol and N_d can be inferred from different SSP scenarios.

It has been documented that sulfate (thus CCN) concentrations are less sensitive to SO_2 precursor emissions under polluted conditions because of the limited availability of oxidants in the atmosphere and the intensive condensation sink of nucleating H_2SO_4 vapour onto existing aerosols[67,68]. Therefore, we use a power-law relationship to describe this nonlinearity. Because non-sulfate aerosols have been found to contribute only minimally to the long-term trends in AOD[69,70] and therefore to AI, only SO_2 emissions are used to predict AI (treated as CCN proxy). In this case, a linear fit on a logarithmic scale is applied:

$$\ln AI = a_1 \ln SO_2 + c \tag{3}$$

For each individual region, the regression models are trained by annual-mean CEDS emissions and MODIS aerosol (2001–2019) and then applied on SSP emissions to predict AI in different future scenarios (2020–2100). Using the CMIP6 model output as a direct source for obtaining aerosol in the near-term future is also an alternative approach; however, considering the incorrect emissions used in CMIP6 models ('Emissions data' section), we choose not to do so here.

Regarding the aerosol-to-N_d relations, both sigmoidal and OLS methods (as detailed earlier) are utilized but with the preference being put on the former. Data used to construct the regressions are one-year (2008) MODIS 5×5 km^2 daily N_d and AI (projected from $1° \times 1°$ without altering the original values) observations over global oceans between 60° S and 60° N, which are carefully filtered for retrieval errors and precipitation to reduce uncertainty. For the OLS method, the data are grouped into 20 AI bins, with each bin having an equal number of samples. The median values of N_d and AI in these bins are then used in OLS regression as in refs. 31 and [32]. As for the sigmoid fit, an AI–N_d joint histogram is constructed first with fixed intervals in a logarithmic scale; then the medians of N_d in each AI interval together with central AI are considered as inputs for the regression.

Given the AI–N_d relationship over land is quite unreliable due to the retrieval issues; for example, even the 'anti-Twomey effect' can be seen from satellites in most continental regions[43,71,72], here we apply the aforementioned AI–N_d relationship over global oceans to different continental regions. Note that using a single global relation would cause differences between observed and predicted N_d for individual regions. This is probably attributable to the varying (1) cloud adiabaticity, (2) surface reflectance and (3) meteorological background across regions, in which (1) and (2) appear to impact N_d retrieval, while (3) reflects the capability of droplet activation. It is also interesting to note that the difference between observed and predicted N_d was found to be close to a certain constant for each region and independent of long-term temporal evolution[30]. Building on this idea, we add a correction constant—that is, defined as the difference in multi-year averaged N_d between observations and predictions—to predicted N_d for each individual region to overcome this issue.

Radiative forcing

From predicted N_d, the change in $\ln N_d$ relative to 2001 ($\Delta \ln N_d$) is computed. On the basis of $\Delta \ln N_d$, the change in cloud albedo is derived using the Twomey formula[73]; then radiative forcing due aerosol–cloud interactions (the Twomey effect; RF_{aci}) relative to 2001 can be thereby computed:

$$RF_{aci} = -F^{\downarrow} f_{liq} \frac{\alpha_{cld}(1 - \alpha_{cld})}{3} \Delta \ln N_d \tag{4}$$

where $F^{\downarrow}$ and α_{cld} are mean incoming solar radiation flux and the cloud albedo from the Clouds and the Earth's Radiant Energy System and f_{liq} is the CF of liquid clouds from the MODIS Level 3 product.

Data availability

The MODIS cloud and aerosol products from Aqua (MYD08_L3 and MYD06_L2) and Terra (MOD08_L3 and MOD06_L2) are available from the Atmosphere Archive and Distribution System Distributed Active Archive Center of National Aeronautics and Space Administration (LAADS-DAAC, NASA) at https://ladsweb.modaps.eosdis.nasa.gov. The CloudSat data are available from http://cloudsat.atmos.colostate.edu/data/. The CERES SSF product is available from https://opendap.larc.nasa.gov/opendap/CERES/SSF/. CEDSv_2021_04_21 emissions are from the PNNL DataHub at https://doi.org/10.25584/PNNLData-Hub/1779095. CMIP6 climate model output is from the Earth System Grid Federation (https://esgf.llnl.gov).

Code availability

The codes for generating the figures in this work are available at https://zenodo.org/record/8128056 (ref. 74).

References

47. Levy, R. C. et al. The collection 6 MODIS aerosol products over land and ocean. *Atmos. Meas. Tech.* **6**, 2989–3034 (2013).
48. Sayer, A. M., Hsu, N. C., Bettenhausen, C. & Jeong, M.-J. Validation and uncertainty estimates for modis collection 6 'deep blue' aerosol data. *J. Geophys. Res. Atmos.* **118**, 7864–7872 (2013).
49. Nakajima, T., Higurashi, A., Kawamoto, K. & Penner, J. E. A possible correlation between satellite-derived cloud and aerosol microphysical parameters. *Geophys. Res. Lett.* **28**, 1171–1174 (2001).
50. Stier, P. Limitations of passive remote sensing to constrain global cloud condensation nuclei. *Atmos. Chem. Phys.* **16**, 6595–6607 (2016).
51. Saponaro, G. et al. Estimates of the aerosol indirect effect over the Baltic Sea region derived from 12 years of MODIS observations. *Atmos. Chem. Phys.* **17**, 3133–3143 (2017).
52. Platnick, S. et al. The MODIS cloud optical and microphysical products: collection 6 updates and examples from Terra and Aqua. *IEEE Trans. Geosci. Remote Sens.* **55**, 502–525 (2017).
53. Quaas, J., Boucher, O. & Lohmann, U. Constraining the total aerosol indirect effect in the LMDZ and ECHAM4 GCMs using MODIS satellite data. *Atmos. Chem. Phys.* **6**, 947–955 (2006).
54. Zhang, Z. & Platnick, S. An assessment of differences between cloud effective particle radius retrievals for marine water clouds from three MODIS spectral bands. *J. Geophys. Res.* **116**, D20215 (2011).
55. Grosvenor, D. P. et al. Remote sensing of droplet number concentration in warm clouds: a review of the current state of knowledge and perspectives. *Rev. Geophys.* **56**, 409–453 (2018).
56. Hoesly, R. M. et al. Historical (1750-2014) anthropogenic emissions of reactive gases and aerosols from the Community Emissions Data System (CEDS). *Geosci. Model Dev.* **11**, 369–408 (2018).
57. Riahi, K. et al. The shared socioeconomic pathways and their energy, land use, and greenhouse gas emissions implications: an overview. *Glob. Environ. Change* **42**, 153–168 (2017).
58. Gidden, M. J. et al. Global emissions pathways under different socioeconomic scenarios for use in CMIP6: a dataset of harmonized emissions trajectories through the end of the century. *Geosci. Model Dev.* **12**, 1443–1475 (2019).
59. Gidden, M. Aneris: harmonization for integrated assessment models. *Zenodo* https://doi.org/10.5281/zenodo.802832 (2017).
60. Gidden, M. J. et al. A methodology and implementation of automated emissions harmonization for use in integrated assessment models. *Environ. Modell. Softw.* **105**, 187–200 (2018).
61. Eyring, V. et al. Overview of the coupled model intercomparison project phase 6 (CMIP6) experimental design and organization. *Geosci. Model Dev.* **9**, 1937–1958 (2016).
62. Gillett, N. P. et al. The detection and attribution model intercomparison project (DAMIP v1.0) contribution to CMIP6. *Geosci. Model Devel.* **9**, 3685–3697 (2016).

63. O'Neill, B. C. et al. The Scenario Model Intercomparison Project (ScenarioMIP) for CMIP6. *Geosci. Model Dev.* **9**, 3461–3482 (2016).

64. Saponaro, G. et al. Evaluation of aerosol and cloud properties in three climate models using MODIS observations and its corresponding COSP simulator, as well as their application in aerosol–cloud interactions. *Atmos. Chem. Phys.* **20**, 1607–1626 (2020).

65. Cleveland, W. S. Robust locally weighted regression and smoothing scatterplots. *J. Am. Stat. Assoc.* **74**, 829–836 (1979).

66. Boucher, O. & Lohmann, U. The sulfate–CCN–cloud albedo effect: a sensitivity study with two general circulation models. *Tellus B Chem. Phys. Meteorol.* **47**, 281–300 (1995).

67. Liu, J., Mauzerall, D. L. & Horowitz, L. W. Source–receptor relationships between East Asian sulfur dioxide emissions and Northern Hemisphere sulfate concentrations. *Atmos. Chem. Phys.* **8**, 3721–3733 (2008).

68. Carslaw, K. S. et al. Large contribution of natural aerosols to uncertainty in indirect forcing. *Nature* **503**, 67–71 (2013).

69. Streets, D. G. et al. Anthropogenic and natural contributions to regional trends in aerosol optical depth, 1980-2006. *J. Geophys. Res. Atmos.* **114**, D00D18 (2009).

70. Rawat, P., Sarkar, S., Jia, S., Khillare, P. S. & Sharma, B. Regional sulfate drives long-term rise in AOD over megacity Kolkata, India. *Atmos. Environ.* **209**, 167–181 (2019).

71. Grandey, B. S. & Stier, P. A critical look at spatial scale choices in satellite-based aerosol indirect effect studies. *Atmos. Chem. Phys.* **10**, 11459–11470 (2010).

72. Gryspeerdt, E. et al. The impact of sampling strategy on the cloud droplet number concentration estimated from satellite data. *Atmos. Meas. Tech.* **15**, 3875–3892 (2022).

73. Twomey, S. Aerosols, clouds and radiation. *Atmos. Environ.* **25**, 2435–2442 (1991).

74. Jia, H. & Quaas, J. Supporting data for 'Nonlinearity of the cloud response postpones climate penalty of mitigating air pollution in polluted regions'. *Zenodo* https://doi.org/10.5281/zenodo.8128056 (2023).

Author contributions

H.J. and J.Q. conceptualized the research. H.J. performed the analysis and prepared the paper with comments from J.Q.

Competing interests

The authors declare no competing interests.

Additional information

Extended data is available for this paper at https://doi.org/10.1038/s41558-023-01775-5.

Supplementary information The online version contains supplementary material available at https://doi.org/10.1038/s41558-023-01775-5.

Correspondence and requests for materials should be addressed to Hailing Jia.

Peer review information *Nature Climate Change* thanks Chaopeng Hong and the other, anonymous, reviewer(s) for their contribution to the peer review of this work.

Reprints and permissions information is available at www.nature.com/reprints.
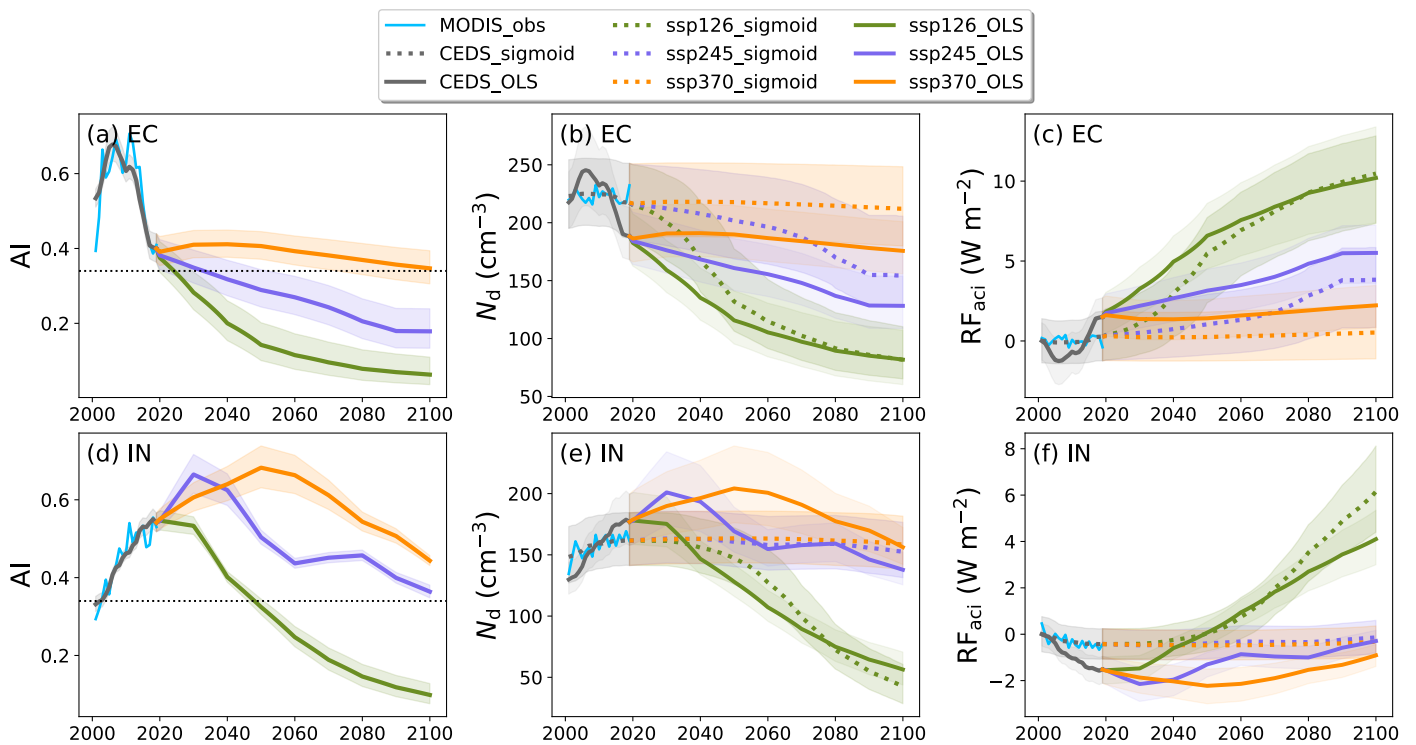
Extended Data Fig. 1 | Observed and predicted aerosol index, cloud droplet number concentration and radiative forcing during 2000–2100 over China and India. a–f, Past and future mean regional changes in AI (**a,d**), N_d (**b,e**) and RF_{aci} (**c,f**) over EC (top) and IN (bottom) diagnosed from past and future aerosol emissions. The figure is the same as Fig. 3, but adding the predictions for SSP2-4.5 scenario in addition to SSP1-2.6 and SSP3-7.0 scenarios.
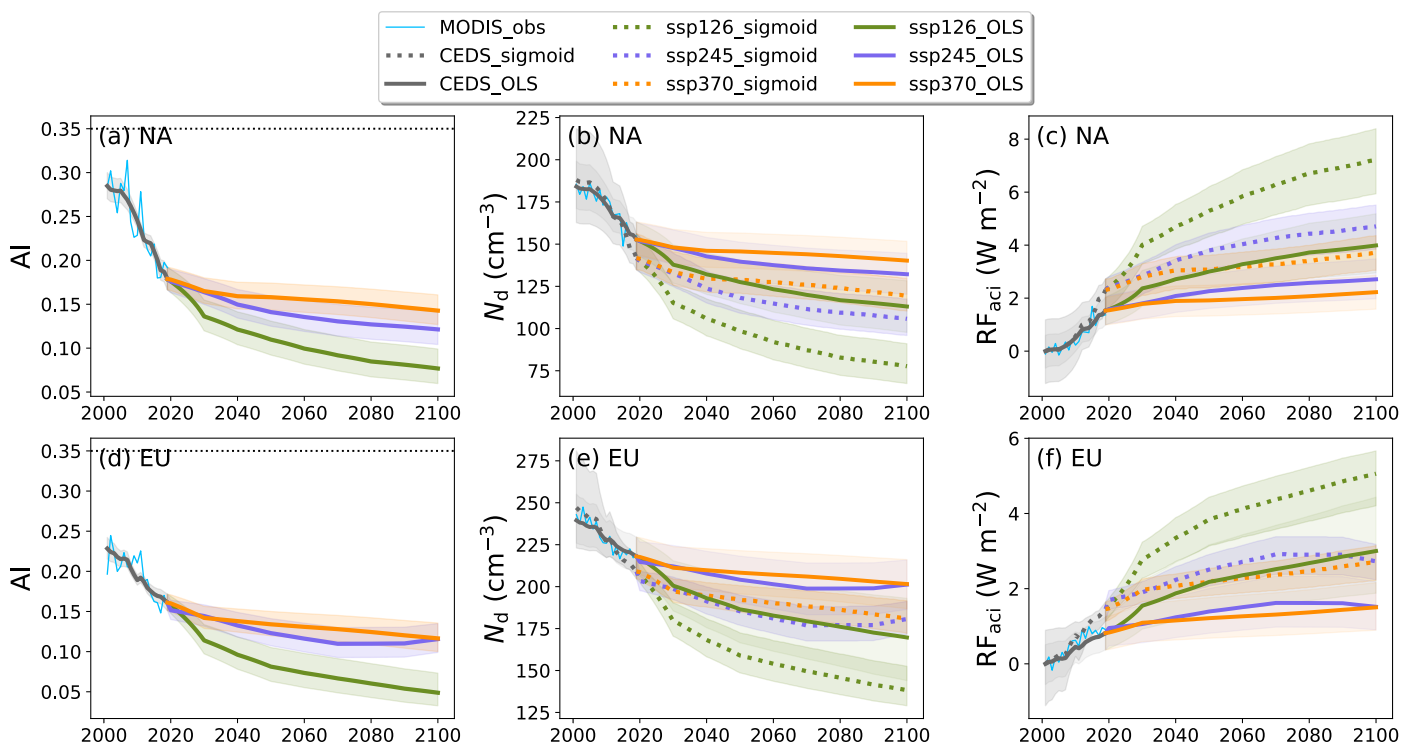
Extended Data Fig. 2 | Observed and predicted aerosol index, cloud droplet number concentration and radiative forcing during 2000–2100 over North America and Europe. a–f, Past and future mean regional changes in AI (**a**,**d**), N_d (**b**,**e**) and RF_{aci} (**c**,**f**) over NA (top) and EU (bottom) diagnosed from past and future aerosol emissions. This figure is the same as Extended Data Fig. 1, but for NA and EU.